Steady-State and Transient Kinetic Analyses of Taurine/α-Ketoglutarate Dioxygenase: Effects of Oxygen Concentration, Alternative Sulfonates, and Active-Site Variants on the Fe^{IV}-oxo Intermediate†

Piotr K. Grzyska,‡ Matthew J. Ryle,‡,§ Greta R. Monterosso,‡ Jian Liu,‡ David P. Ballou,‖ and Robert P. Hausinger*,‡

Department of Microbiology and Molecular Genetics and Department of Biochemistry and Molecular Biology, Michigan State University, East Lansing, Michigan 48824-4320, and Department of Chemistry, Division of Biophysics, University of Michigan, Ann Arbor, Michigan 48109-1055

Received June 16, 2004; Revised Manuscript Received December 13, 2004

ABSTRACT: Taurine/α-ketoglutarate (αKG) dioxygenase (TauD), an archetype αKG-dependent hydroxylase, is a non-heme mononuclear Fe^{II} enzyme that couples the oxidative decarboxylation of αKG with the conversion of taurine to aminoacetaldehyde and sulfite. The crystal structure of taurine-αKG-Fe^{II}TauD is known, and spectroscopic studies have kinetically defined the early steps in catalysis and identified a high-spin Fe^{IV}-oxo reaction intermediate. The present analysis extends our understanding of TauD catalysis by investigating the steady-state and transient kinetics of wild-type and variant forms of the enzyme with taurine and alternative sulfonates. TauD proteins substituted at residues surrounding the active site were shown to fold properly based on their abilities to form a diagnostic chromophore associated with the anaerobic Fe^{II}-αKG chelate complex and to generate a tyrosyl radical upon subsequent reaction with oxygen. Steady-state studies of mutant proteins confirmed the importance of His 70 and Arg 270 in binding the sulfonate moiety of taurine and indicated the participation of Asn 95 in recognizing the substrate amine group. The N97A and S158A variants are likely to undergo an increase in hydrophobicity and expansion of the substrate-binding pocket, thus accounting for their decreased K_m toward pentanesulfonic acid compared to wild-type TauD. Stopped-flow UV−visible spectroscopic examination of the reaction of oxygen with taurine-αKG-Fe^{II}TauD confirmed a minimal three-step sequence of reactions attributed to Fe^{IV}-oxo formation (k_1), bleaching to the Fe^{II} state upon substrate hydroxylation (k_2), rebinding of excess substrates (k_3), and indicated that none of the steps exhibit detectable solvent k_H/k_D isotope effects. This demonstrates that no protons are involved in the rate-determining step of Fe^{IV}-oxo formation, in contrast to heme iron oxygenases. The Fe^{IV}-oxo species is likely to be utilized in conversion of the alternative substrates pentanesulfonic acid and 3-*N*-morpholinopropanesulfonic acid; however, this spectroscopic intermediate was not detected because of the decreased k_1/k_2 ratio. With taurine, k_1 was shown to depend on the oxygen concentration allowing calculation of a second-order rate constant of $1.58 \times 10^5\ M^{-1}\ s^{-1}$ for this irreversible reaction. Stopped-flow analyses of TauD variants provided several insights into how the protein environment influences the rates of Fe^{IV}-oxo formation and decay. The Fe^{IV}-oxo species was not detected in the N95D or N95A variants because of a reduced k_1/k_2 ratio, likely related to a decreased substrate-dependent conversion of the six-coordinate to five-coordinate metal site.

α-Ketoglutarate (αKG)[1]-dependent dioxygenases are mononuclear, non-heme Fe^{II} enzymes that couple the oxidative decarboxylation of an α-ketoacid to the oxidation of a target substrate (*1*, *2*). Hydroxylation reactions catalyzed by members of this enzyme superfamily are used to repair alkylation damage to DNA and RNA (*3*, *4*), modify structural proteins (*5*), regulate hypoxia-induced transcription factor levels (*6*−*8*), synthesize antibiotics (*9*, *10*), generate plant flavonoids, gibberellins, and alkaloids (*11*−*14*), metabolize phytanic acid (*15*), degrade herbicides (*16*), and carry out a wide range of other biological conversions. In addition to these hydroxylation reactions, Fe^{II}/αKG-dependent dioxygenases and related enzymes are known to function in ring formation, ring expansion, desaturation, and other types of oxidative transformations (*1*, *9*, *17*−*21*). The focus of the studies described here is the *Escherichia coli* enzyme taurine/αKG dioxygenase (TauD), which decomposes taurine (2-aminoethanesulfonate) as a sulfur source to produce aminoacetaldehyde and sulfite (Scheme 1) (*22*).

† These studies were supported by the National Institutes of Health (Postdoctoral Fellowship GM20196 to M.J.R., Grant GM20877 to D.P.B., and Grant GM063584 to R.P.H.). R.P.H. dedicates this contribution to Professor Chris Walsh on the occasion of his 60th birthday.

* To whom correspondence should be addressed. Telephone: 517-355-6463 ext. 1610. Fax: 517-353-8957. E-mail: hausinge@msu.edu.

‡ Michigan State University.

§ Current address: Idexx Laboratories, One Idexx Drive, Westbrook, ME 04092.

‖ University of Michigan.

[1] Abbreviations: aKG, α-ketoglutarate; MOPS, 3-*N*-morpholinopropanesulfonic acid; PSA, pentanesulfonic acid; TauD, taurine/αKG dioxygenase.

10.1021/bi048746n CCC: $30.25
Published on Web 02/18/2005

Scheme 1

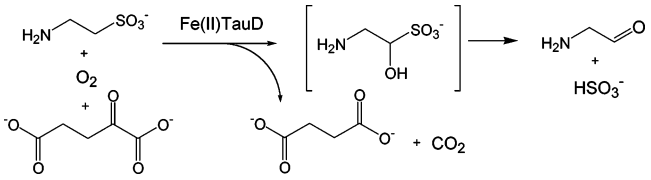

Scheme 2

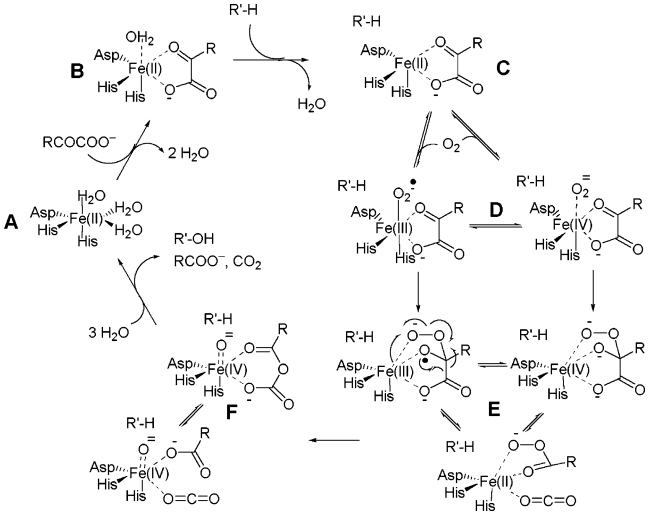

The generally reported mechanism for Fe^{II}/αKG-dependent hydroxylases (*1*, *23*), first proposed over 20 years ago (*24*), is illustrated in Scheme 2. Resting enzyme (**A**) contains an Fe^{II} center that is ligated by two histidines and one aspartate (or in some cases glutamate), with three water molecules completing the six-coordinate environment. The α-ketoacid binds directly to the Fe^{II} center through its C-1 carboxylate and C-2 carbonyl moieties, thus displacing two water molecules, while maintaining a six-coordinate Fe^{II} center (**B**). The primary substrate binds near the active site and promotes dissociation of the remaining water ligand, leaving the Fe^{II} five-coordinate (**C**) and primed to react with oxygen. Binding of oxygen produces an Fe^{III}-superoxo or Fe^{IV}-peroxo species (**D**) that attacks the αKG carbonyl group (**E**), leading to decomposition of αKG and heterolytic O−O bond cleavage. The resulting Fe^{IV}-oxo species (**F**) inserts oxygen into the target C−H bond of the substrate by hydrogen atom transfer and oxygen rebound, as found in heme-type oxygenases (*25*), to restore the Fe^{II} state of the enzyme (**A**).

Several lines of evidence support the general proposal shown in Scheme 2. Crystallographic structures of *E. coli* TauD (*26*, *27*), *Streptomyces clavuligerus* deacetoxycephalosporin C synthase (*17*, *28*), *S. clavuligerus* clavaminate synthase (*9*, *29*), *Streptomyces* sp. strain TH1 proline 3-hydroxylase (*10*), *Arabidopsis thaliana* anthocyanidin synthase (*18*), human hypoxia-inducible factor-specific asparaginyl hydroxylase (*8*, *30*), *Erwinia carotovora* carbapenem synthase (*21*), and *Pseudomonas putida* S-313 alkylsulfatase (*31*) identify the protein side chains coordinating the metal, define the chelate-binding structure of αKG, and (in some cases) indicate how the primary substrate binds to the corresponding protein. The αKG-Fe^{II} complex formed in these enzymes exhibits diagnostic metal-to-ligand charge-transfer transitions ($\lambda_{max} = 530$ nm and $\epsilon_{530} = 140$ M^{-1} cm^{-1} in the case of TauD) that can be used to monitor αKG binding (*32*). Interactions with the primary substrate induce a switch from six-coordinate to five-coordinate metal geometry as deduced from changes to the clavaminate synthase magnetic circular dichroism spectra (*33*, *34*), perturbations of the UV−visible spectra (yielding $\lambda_{max} = 520$ nm and $\epsilon_{520} = 180$ M^{-1} cm^{-1} in the case of TauD) (*32*), and alteration of resonance Raman spectra (also carried out with TauD) (*35*). Stopped-flow UV−visible spectroscopy, coupled with freeze-quench Mössbauer analyses and electron paramagnetic resonance studies, reveals a novel high-spin Fe^{IV} intermediate (with difference spectra revealing $\lambda_{max} = 318$ nm and $\epsilon_{318} = 1500$ M^{-1} cm^{-1}) during the reaction of taurine-αKG-Fe^{II}-TauD with oxygen (*36*). On the basis of its 37-fold decrease in the decay rate when using deuterated substrate (*37*), this intermediate is considered to be responsible for hydrogen atom abstraction. Continuous-flow resonance Raman difference spectra (obtained for the intermediate generated with $^{16}O_2$ minus that using $^{18}O_2$ at cryogenic temperatures) provide compelling support for an Fe^{IV}-oxo intermediate under these conditions, with a possible metal-hydroperoxo (or metal-alkylperoxo) species also detected (*38*). Evidence derived by extended X-ray absorption fine structure spectroscopy is also consistent with formation of an Fe^{IV}-oxo species in TauD (*39*). More broadly, the generation of an Fe^{IV}-oxo intermediate is supported by hybrid density function calculations of clavaminate synthase (*40*) and by biomimetic studies that confirm the ability to synthesize a mononuclear, low-spin Fe^{IV}-oxo site in a non-porphyrin ligand environment (*41*, *42*). Spectroscopic and quantum chemical characterization of one such complex has provided additional insight into the iron−oxo bond of the Fe^{IV}-oxo species (*43*). This highly reactive intermediate likely accounts for the observed aromatic side-chain self-hydroxylation reactions of the herbicide-degrading TfdA (*44*), the DNA repair enzyme AlkB (*45*), and TauD (*46*, *47*). Analogous chemistry might also occur in 4-hydroxyphenylpyruvate dioxygenase (*48*−*51*), another Fe^{II}- and α-keto-acid-dependent enzyme which is unrelated in sequence and functions in tyrosine catabolism.

The studies described here extend the analysis of TauD kinetic properties in several new directions. First, we characterize the steady-state kinetic properties of a series of active-site variants of TauD that were designed on the basis of the TauD crystal structure (*26*, *27*), illustrated in Figure 1. These studies confirm that His 70 and Arg 270 are necessary to bind the taurine sulfonate moiety and that Asn 95 is important for interacting with the taurine amino group. Second, we examine the steady-state kinetics of wild-type TauD and selected variants with two slow-reacting alternative substrates, 3-*N*-morpholinopropanesulfonic acid (MOPS) and pentanesulfonic acid (PSA). This work demonstrates that the enzyme can be manipulated to have improved catalytic efficiencies with alternative substrates. Third, we examine the transient kinetics associated with wild-type TauD and report that the apparent rate constants do not exhibit detectable solvent k_H/k_D isotope effects. This finding demonstrates that no protons are involved in the rate-determining step of Fe^{IV}-oxo formation, a situation that is distinct from that observed in cytochrome P450 enzymes. Fourth, we show that significant levels of the Fe^{IV}-oxo species do not form when using alternative substrates, probably because of the low rate constant of Fe^{IV}-oxo formation. Fifth, we demonstrate that the rate of formation of the Fe^{IV}-oxo species

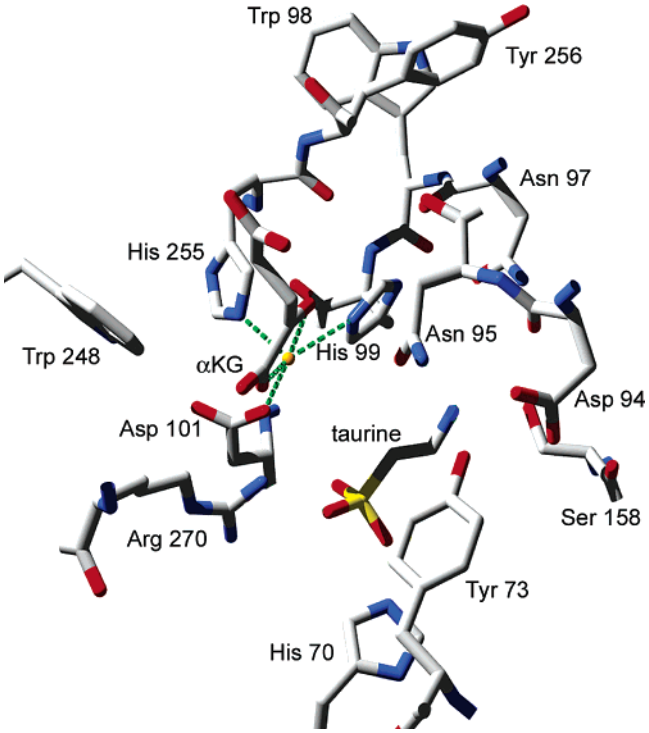

FIGURE 1: TauD active site. A model of the 2.5 Å resolution crystal structure of taurine-αKG-Fe^{II}TauD (*27*) reveals the Fe^{II} ligands (αKG, Asp 101, His 98, and His 255), two Trp residues near the metal center (Trp 98 and Trp 248), and selected other residues near the taurine-binding site.

depends on the oxygen concentration, allowing calculation of the second-order rate constant of oxygen binding and the first-order rate constant of its dissociation. Finally, we compare the stopped-flow kinetics of selected variant enzymes to gain some insights into how the protein environment influences the rate constants associated with the Fe^{IV}-oxo species.

EXPERIMENTAL PROCEDURES

Enzyme Purification and Assays. Wild-type and altered forms of TauD were purified as previously described (*46*). For detailed steady-state kinetic analyses, enzyme assays were carried out using time points from 10 s to 5 min and the sulfite production progress curves were analyzed by fitting the data to the equation

$$P_t = v_i(1 - \exp(-k_{inact}t))k_{inact}^{-1} \quad (1)$$

where P_t is the accumulated product at time t, v_i is the initial rate, and k_{inact} is the inactivation rate constant (*52*). TauD is known to undergo irreversible inactivation during catalysis using taurine (*46*); thus, complete kinetic analysis of TauD and its variants with taurine and other sulfonates requires comparison of k_{inact} values. For routine studies, kinetic constants for taurine, MOPS, and PSA were determined by evaluating the sulfite produced after 5 min, and the data were fit to the Michaelis−Menten equation. Assays were carried out at pH 8.0 in 5 mM Tris buffer or at pH 6.9 in 10 mM imidazole buffer at 30 °C.

Site-Directed Mutagenesis. The H70A, Y73S, D94A, N95A, N95D, N97A, W98I, S158A, W248F, Y256I, and R270K variants of TauD were created by mutagenesis of *tauD* in pME4141 (*22*) using the Stratagene Quickchange System (Stratagene, La Jolla, CA) as previously described for the Y256F and Y73I variants (*46*). Mutated plasmids were purified using the QIAprep Spin miniprep kit (Qiagen Sciences, Valencia, CA) and subcloned into *E. coli* DH5α (Invitrogen, Carlsbad, CA). Each mutation was confirmed by sequence analysis (Davis Sequencing, Davis, CA).

Spectroscopy. Anaerobic samples of αKG-Fe^{II}TauD and taurine-αKG-Fe^{II}TauD were prepared (2 mM αKG, 550 μM TauD subunit, and 500 μM Fe^{II} in 25 mM Tris buffer at pH 8.0 containing 0, 2, or 5 mM taurine) for the wild-type and variant enzymes, and UV−visible spectra were recorded at room temperature as previously described (*32*). To assess the effects of MOPS and PSA on the αKG-Fe^{II}TauD spectra, these reagents (from 100 mM anaerobic stock solutions) were added to analogous αKG-Fe^{II}TauD samples and the spectra were recorded. All spectra were corrected to account for sample dilutions. TauD variants were monitored for their ability to form a tyrosyl radical as previously described for the wild-type enzyme; anaerobic solutions of αKG-Fe^{II}TauD (2 mM αKG, 500 μM Fe^{II}, and 550 μM TauD subunit in 25 mM Tris buffer at pH 8.0) were mixed with equal volumes of 100% oxygen-saturated buffer at room temperature, and the UV−visible spectra were recorded after ~8 s.

Stopped-flow UV−visible spectra were obtained by using an Olis RSM-16 UV−visible stopped-flow spectrophotometer (0.4 cm path cell) or a Hi-Tech Scientific model SF-61DX stopped-flow spectrophotometer (1.0 cm path length) in single-mixing mode. Oxygen was removed from the Olis instrument by flushing with 100 mM dithionite and rinsing with several milliliters of anaerobic, 25 mM Tris buffer at pH 8.0. The Hi-Tech apparatus was made anaerobic by flushing the flow system with an anaerobic buffer solution consisting of 0.1 unit/mL of protocatechuic acid dioxygenase and 400 μM protocatechuic acid at pH ~7 (*53*). This solution was allowed to stand in the flow system overnight, and then the flow unit was thoroughly rinsed with anaerobic buffer before experiments. Enzyme and substrate solutions were placed in glass tonometers and made anaerobic by equilibration with oxygen-free argon that has been passed through an Oxyclear oxygen removal column (Labclear). One syringe contained 10 mM taurine, 10 mM αKG, concentrations of Fe^{II} and TauD as noted in the individual studies, and 25 mM Tris buffer at pH 8.0, whereas the other syringe contained buffer that had been saturated with the selected concentration of oxygen (100, 50, 21, 10, or 5%) at room-temperature resulting in oxygen concentrations of 1.15, 0.575, 0.242, 0.115, and 0.058 mM. The experiments were carried out at 4 °C. Experiments with MOPS and PSA were performed as described above, except that the concentrations of these reactants (before mixing) were varied between 10 and 40 mM. TauD variants were analyzed as for the wild-type enzyme. Where noted, the initial concentration of taurine was increased for selected variants. The experimental data for the Olis stopped-flow kinetic measurements were fitted by global analysis using GlobalWorks software (On Line Instrument System, Inc., Jefferson, GA) (*54*), providing singular value decomposition spectra corresponding to the global changes in absorbance of each phase of the reaction. Apparent rate constants from kinetic traces on the Hi-Tech instrument were calculated from exponential fits using

Table 1: Kinetic and Spectroscopic Parameters for Wild-Type TauD and Selected Variants[a]

TauD variant	k_{cat} (s^{-1})	taurine K_m (μM)	k_{cat}/K_m (μM^{-1} s^{-1})	k_{inact} (s^{-1})	αKG[b] ϵ_{520} M^{-1} cm^{-1}	taurine/αKG[c] ϵ_{520} M^{-1} cm^{-1}
wild type	12.5 ± 0.5	58 ± 6	0.22 ± 0.03	0.0032 ± 0.0007	240	270
H70A					230	230
Y73I	7.3 ± 0.6	243 ± 33	0.030 ± 0.007	0.013 ± 0.001	260	290
Y73S	11.0 ± 2.0	630 ± 200	0.018 ± 0.009	0.0018 ± 0.0004	240	257
D94A	6.6 ± 0.7	52 ± 7	0.13 ± 0.03	0.009 ± 0.002	240	270
N95A	0.83 ± 0.05	1500 ± 600	0.0006 ± 0.0003	0.010 ± 0.005	200	200
N95D	1.75 ± 0.7	1500 ± 300	0.0012 ± 0.0007	0.0057 ± 0.0033	210	220
N97A	3.8 ± 0.5	44 ± 17	0.09 ± 0.04	0.0037 ± 0.0013	240	270
W98I	15.1 ± 1.2	75 ± 30	0.20 ± 0.10	none detected	140	240
S158A	6.3 ± 0.8	100 ± 20	0.06 ± 0.02	0.0028 ± 0.0017	230	270
W248F	4.55 ± 0.4	100 ± 30	0.046 ± 0.017	0.0032 ± 0.0017	220	260
Y256F	6.2 ± 0.3	122 ± 17	0.05 ± 0.01	0.0087 ± 0.0012	220	260
R270K					220	220

[a] Analyzed at pH 8.0 and 30 °C using taurine as the substrate. [b] Extinction coefficient at 520 nm for the chromophore associated with the anaerobic αKG-Fe^{II}TauD protein. [c] Extinction coefficient at 520 nm for the anaerobic taurine-αKG-Fe^{II}TauD samples.

KinetAsyst3 software (Hi-Tech Scientific, Salisbury, U.K.) and Program A (see below).

^2H_2O Solvent Isotope Effect. For examination of solvent isotope effects, the enzyme was lyophilized, dissolved in buffer (>95% ^2H_2O), and mixed with other reagents similarly prepared in ^2H_2O. The p^{2}H values were determined by adding 0.4 to the pH electrode reading (*55*).

Simulations. Kinetic traces from the stopped-flow spectrophotometers were simulated by models of consecutive functions using Program A (developed by Chung-Yen Chiu, Rong Chang, and Joel Dinverno under the direction of David P. Ballou, University of Michigan) based on the Marquardt−Levenberg nonlinear fit algorithm (*56*). The simulations allowed estimation of rate constants and extinction coefficients and provided insight into the confidence of these estimated values.

RESULTS

Spectroscopic Characterization of Active-Site Variants of TauD. To confirm proper folding of the TauD variants, each mutant protein was examined for its ability to generate αKG-Fe^{II}TauD, taurine-αKG-Fe^{II}TauD, and tyrosyl radical chromophores (*32*, *46*). As shown in Table 1, all variant proteins produced the diagnostic metal-to-ligand charge-transfer spectra that arise from αKG chelation of protein-bound metal in the absence and presence of taurine. The absorbance intensity of the αKG-Fe^{II}W98I variant is approximately half of that shown for other proteins in the table. This result is shown in the spectrum of the αKG-Fe^{II}W98I protein (black trace of Figure 2B) in comparison to those of the N95D and Y256F variants (black traces of parts A and C of Figure 2, respectively) or wild-type enzyme (black trace of Figure 3). Anaerobic addition of taurine to the αKG-bound mutant protein samples (blue traces of Figure 2) yielded spectra that all resembled that of the taurine- and αKG-bound wild-type enzyme (blue trace of Figure 3A). The enhancement in absorbance for the αKG-Fe^{II}TauD W98I sample upon adding taurine is reminiscent of the behavior reported for α-ketoadipate and taurine binding to the wild-type enzyme (*32*). As in that case, the chromophore intensity changes may be attributed to taurine enforcing a constraint on the bound α-ketoacid to enhance the absorbance of the metallocenter complex. The three electronic transitions of the N95D and Y256F spectra were less distinct than those observed in the other samples, and the spectral maxima of these enzymes did not shift as notably as for most other samples. Also of significance, the R270K and H70A variants failed to undergo a taurine-induced change in their spectra.

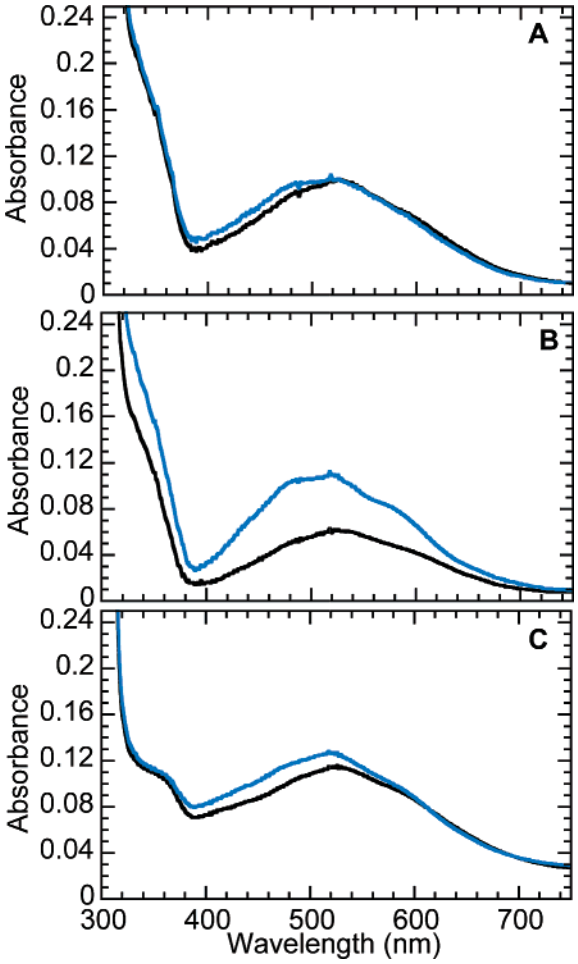

FIGURE 2: Effect of taurine addition on the absorbance spectra of the αKG- and Fe^{II}-bound states of selected variants. Anaerobic samples of the (A) N95D, (B) W98I, and (C) Y256F variants of TauD (550 μM subunit) were adjusted to contain 500 μM Fe^{II} and 2 mM αKG in 25 mM Tris buffer at pH 8.0 (black traces). Subsequent addition of taurine (5, 2, and 2 mM, respectively) resulted in spectra shown by the blue traces.

The Fe^{II}- and αKG-bound form of wild-type TauD (i.e., enzyme-lacking taurine) is known to react with oxygen to

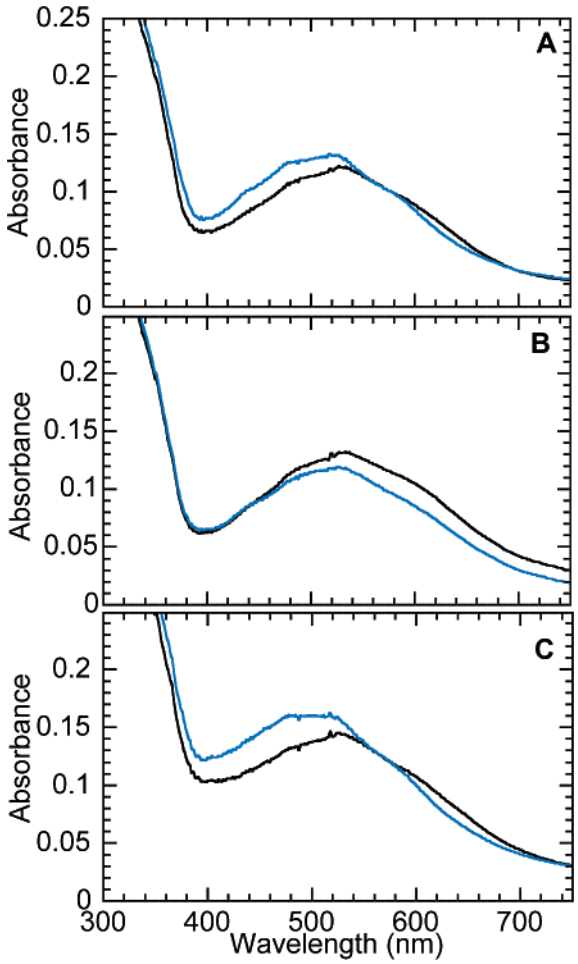

FIGURE 3: Perturbations to the absorbance spectrum of anaerobic αKG-Fe^{II}TauD (black traces) by addition of (A) taurine, (B) PSA, and (C) MOPS (blue traces). The final reactant concentrations were 550 μM TauD subunit, 500 μM Fe^{II}, 2 mM αKG, and either 2 mM taurine, 5 mM PSA, or 2 mM MOPS, in 25 mM Tris buffer at pH 8.0.

form a transient tyrosyl radical involving Tyr 73 that exhibits an absorbance at 408 nm (*46*). It is likely that this tyrosyl radical is produced by reaction of the tyrosine with a highly oxidizing species such as Fe^{IV}-oxo. Therefore, to assess whether the variant proteins were capable of reacting with oxygen to produce such a species, they were tested for their ability to carry out this chemistry. With the exception of the Tyr 73 variants, all of the proteins listed in Table 1 formed the tyrosyl radical when the Fe^{II} forms of the mutant enzymes were mixed with oxygen in the presence of αKG (data not shown). The tyrosyl radical did not form in the presence of the substrate, except with the H70A and R270K variants. Normally, the highly oxidizing Fe^{IV}-oxo intermediate reacts with substrates, but when no substrate is present, it abstracts an electron or hydrogen atom from a nearby tyrosyl residue. The H70A and R270K variants do not bind taurine, so that the tyrosyl radical is formed, even in the absence of taurine. The capacity of the mutant proteins to generate the αKG-bound chromophore confirms that they fold correctly and their ability to form a tyrosyl radical demonstrates their capacity to activate oxygen.

Steady-State Kinetic Properties of Active-Site Variants of TauD. The TauD active-site variants were examined for their steady-state kinetic properties and rates of inactivation (Table 1). Alteration of residues that are proposed to interact with the sulfonate moiety of taurine [His 70 and Arg 270 based on structural results (*26*, *27*)] eliminated the production of sulfite. Substitution of Asn 95 with Ala or Asp caused a large increase in the K_m of taurine, consistent with this residue being important for taurine recognition. The Y73S enzyme had an 11-fold increase in taurine K_m compared to wild-type TauD, and the Y73I, S158A, W248F, and Y256F variants exhibited ~2-fold increases, while the other variants shown in Table 1 had negligible influence on this parameter. Notably, the Y73I, D94A, N95A, N95D, and Y256F variants were found to inactivate more rapidly than the wild-type enzyme. Conversely, enzyme inactivation was less in the Y73S protein and not detected in the W98I variant. All variants were diminished in their catalytic efficiency (k_{cat}/K_m) compared to the wild-type enzyme (Table 1).

Spectroscopic Characterization and Steady-State Kinetic Properties of TauD with Alternative Sulfonates. MOPS and PSA are known to be substrates of TauD (*22*). The addition of MOPS to anaerobic αKG-Fe^{II}TauD increased the absorbance and shifted the maximum to a shorter wavelength (Figure 3C), analogous to the spectral change produced by addition of taurine (Figure 3A). In contrast, absorbance changes were less evident for PSA (added at 5 or 20 mM concentrations, resulting in equivalent spectra), as illustrated in Figure 3B. We attribute the near identity of spectra in the absence and presence of PSA to the retention of six-coordinate geometry of the metal because of continued coordination of water when PSA is present.

Prior steady-state kinetic studies of wild-type TauD (*22*) yielded values of K_m for MOPS (145 μM) and PSA (590 μM) that were higher than for taurine (55 μM) and showed that these alternative sulfonates turn over about half as fast as the normal substrate (2.0 and 1.9 μmol min^{-1} (mg protein)$^{-1}$ versus 4.1 μmol min^{-1} (mg protein)$^{-1}$, corresponding to k_{cat} values of 1.1, 1.0, and 2.2 s^{-1}). All of the previously reported values were obtained at 30 °C and pH 6.9. We reevaluated the kinetics of PSA and MOPS transformation using the same conditions as well as using pH 8.0 buffer (for comparison to the stopped-flow spectroscopic studies at pH 8.0, described below), analyzing the wild-type protein and two variants (Table 2). Surprisingly, the K_m values determined for wild-type enzyme at pH 6.9 using MOPS and PSA (300 and 1700 μM) were significantly higher than those reported previously (*22*) for these conditions, whereas the values for taurine were similar. While our k_{cat} values are very close to those published earlier for MOPS and PSA, our value for taurine is nearly 5-fold greater. The kinetic parameters, including k_{inact}, are only minimally affected by pH at the values chosen for the experiments.

On the basis of the TauD structure (Figure 1), the N97A and S158A variants may be expected to possess larger active-site pockets and thereby facilitate binding of larger substrates. As summarized in Table 2, these variants exhibited slightly decreased K_m and increased catalytic efficiency values for the larger substrate PSA at both pH conditions compared to the wild-type enzyme. In contrast, the N97A and S158A variants resembled the wild-type enzyme in their interactions with MOPS.

Stopped-Flow Analysis of Wild-Type TauD. Previous stopped-flow investigations of the reaction of wild-type taurine-αKG-Fe^{II}TauD with oxygen identified a three-step

Table 2: Comparison of Steady-State Kinetic Parameters for Selected TauD Variants Using Alternative Sulfonates at Two pH Values[a]

substrate (pH) and TauD variant	k_{cat} (s^{-1})	K_m (μM)	k_{cat}/K_m (μM^{-1} s^{-1})	k_{inact} (s^{-1})
taurine (6.9) wild type	10.4 ± 2.7	76 ± 24	0.14 ± 0.08	0.0034 ± 0.003
taurine (6.9) N97A	3.7 ± 1.2	60.2 ± 4.9	0.061 ± 0.024	0.0058 ± 0.0017
taurine (6.9) S158A	7.2 ± 0.05	323 ± 26	0.022 ± 0.003	0.0058 ± 0.0012
taurine (8.0) wild type	12.5 ± 0.5	58 ± 6	0.22 ± 0.03	0.0032 ± 0.0007
taurine (8.0) N97A	3.8 ± 0.5	44 ± 17	0.09 ± 0.04	0.0037 ± 0.0013
taurine (8.0) S158A	6.3 ± 0.8	100 ± 20	0.06 ± 0.2	0.0028 ± 0.0017
PSA (6.9) wild type	2.1 ± 0.6	1700 ± 300	0.0012 ± 0.0005	0.0038 ± 0.0018
PSA (6.9) N97A	1.7 ± 0.2	630 ± 270	0.0026 ± 0.0014	0.0057 ± 0.0008
PSA (6.9) S158A	3.97 ± 1.0	602 ± 274	0.0065 ± 0.0045	0.0062 ± 0.0015
PSA (8.0) wild type	3.5 ± 1.3	2600 ± 500	0.0013 ± 0.0006	0.0042 ± 0.0017
PSA (8.0) N97A	2.83 ± 1.25	1100 ± 300	0.0025 ± 0.0005	0.0037 ± 0.0008
PSA (8.0) S158A	3.00 ± 0.90	900 ± 200	0.0045 ± 0.0003	0.0035 ± 0.0007
MOPS (6.9) wild type	0.95 ± 0.03	300 ± 90	0.0031 ± 0.0010	0.0026 ± 0.0010
MOPS (6.9) N97A	0.59 ± 0.25	236 ± 136	0.0025 ± 0.0024	0.0035 ± 0.0026
MOPS (6.9) S158A	1.25 ± 0.10	247 ± 68	0.0050 ± 0.0013	0.0030 ± 0.0015
MOPS (8.0) wild type	1.7 ± 0.7	440 ± 170	0.0039 ± 0.0026	0.0037 ± 0.0013
MOPS (8.0) N97A	1.83 ± 0.63	960 ± 250	0.0018 ± 0.0010	0.0052 ± 0.0030
MOPS (8.0) S158A	1.67 ± 0.22	480 ± 140	0.0033 ± 0.0003	0.0040 ± 0.0017

[a] Conditions were the same as for Table 1, except for the identity of the sulfonate.

Scheme 3

$$\mathrm{I} \xrightarrow{k_1} \mathrm{II} \xrightarrow{k_2} \mathrm{III} \xrightarrow{k_3} \mathrm{IV}$$

sequence of reactions (Scheme 3, with species IV = species I) in which the initial samples (exhibiting 520 nm absorbance) converted at a second-order rate constant k_1 to an Fe^{IV}-oxo intermediate (with λ_{max} of 318 nm and a shoulder at ~500 nm), followed by generation of a bleached Fe^{II} species associated with a first-order rate constant of k_2, and subsequent restoration of the 520 nm absorbance as the substrates rebind when oxygen is depleted with apparent rate constant k_3 (*36*, *37*).

The three-step sequence of reactions is illustrated in Figure 4 for an anaerobic sample that was mixed with buffer containing 1.15 mM oxygen (such that the final concentrations of enzyme active sites and oxygen are approximately equivalent, with excess αKG and taurine) at 4 °C and monitored at 365 and 520 nm. The steps associated with k_1 and k_2 are most easily observed as the increase and decrease in absorbance at 365 nm. The data at 520 nm show the step associated with k_2 as a decrease in absorbance and that with k_3 as an increase. As shown, simulations of these data according to Scheme 3 using rate constants of 158 000 M^{-1} s^{-1} and 12 and 7 s^{-1} reproduced the experimental traces. The initial extinction coefficients used in the simulations (289 and 246 M^{-1} cm^{-1}) were consistent with the spectrum of Figure 3A and the 520 nm value of Table 1. The small upward deviation at ~0.2 s in the 365 nm trace (where the simulation does not fit well) likely arises from a small proportion of the sample undergoing more than one turnover (*vide infra*). Analogous transient kinetic studies of the taurine-αKG-Fe^{II}TauD reactivity with oxygen were carried out in ^2H_2O at 4 °C (pH 8.34). The data were essentially indistinguishable from those carried out in H_2O, and rate constants derived by simulations revealed no detectable differences beyond experimental uncertainty (data not shown).

When the reaction was monitored with limiting concentrations of substrates over a series of wavelengths between 315 and 365 nm, each trace exhibited the same kinetics of formation and decay of the Fe^{IV}-oxo intermediate and the small upward deviation at ~0.2 s was not observed (Figure 5). The identity in apparent rate constants is significant because it argues against the possibility that multiple intermediates with overlapping absorbance features are formed during this reaction.

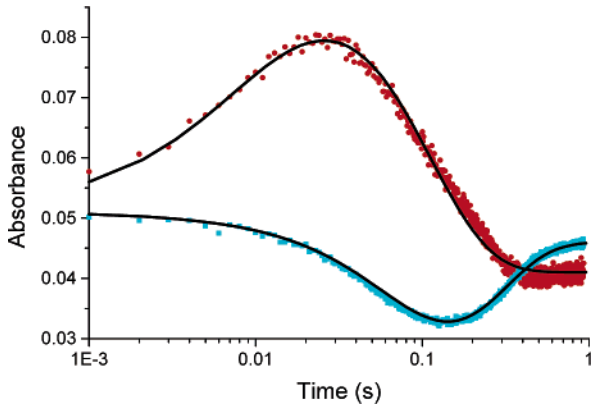

FIGURE 4: Detection at two wavelengths and simulations of the stopped-flow UV−visible kinetics of wild-type TauD. Spectra were obtained after mixing 1.1 mM TauD subunit, 1.0 mM Fe^{II}, 10 mM αKG, and 10 mM taurine in 25 mM Tris buffer at pH 8.0, with an equal volume of buffer containing 1.15 mM oxygen. The experimental data (0.4 cm path length using the Olis instrument) at 365 nm (red dots) and 520 nm (cyan squares) are compared with the simulated three-step time courses (black lines) that were generated by using the parameters shown in the text.

The rates of Fe^{IV}-oxo formation and decay were examined for the wild-type enzyme as a function of the oxygen concentration. To examine a wide range of oxygen concentrations, some of these experiments utilized low concentrations of enzyme, resulting in traces that exhibited complications at times greater than ~0.2 s because of additional turnovers (upper panel of Figure 6). Thus, values of k_3, the apparent rate constant associated with the third phase of turnover, were obscured, and the final decreases in absorbance at 320 nm and increases at 520 nm indicate the return to the substrate-bound form of the enzyme when oxygen was depleted. Nevertheless, from these and other experiments,

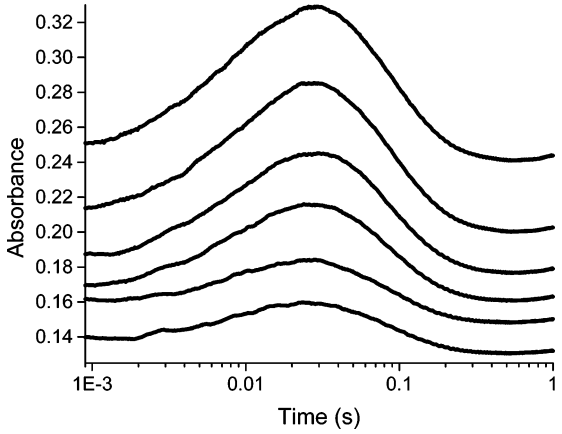

FIGURE 5: Stopped-flow UV−visible kinetics of the Fe^{IV}-oxo intermediate monitored at varied wavelengths. An anaerobic solution containing 250 μM TauD, 200 μM Fe^{II}, 250 μM αKG, and 250 μM taurine in 25 mM Tris buffer at pH 8.0 was mixed with an equal volume of buffer equilibrated with 1.15 mM O_2, and the absorbance intensities were monitored at 315, 320, 330, 340, 360, and 365 nm (top−bottom, 1 cm path length using the Hi-Tech instrument).

the apparent first-order rate constants of Fe^{IV}-oxo formation (k_1) and decay (k_2) could be estimated for several enzyme concentrations (lower panel of Figure 6). The observed rate constants of Fe^{IV}-oxo formation are directly dependent on the oxygen concentration, whereas the rate constant of Fe^{IV}-oxo decay was not (as evident from the upper panel of Figure 6; the points associated with the decay rates at the lowest oxygen concentrations, which approximate the enzyme concentration, are not well-determined).

To better understand the results depicted in the lower panel of Figure 6, apparent rate constants were estimated by simulating kinetic traces generated by using the three-step consecutive model (Scheme 3). For example, we used k_1 of 158 000 M^{-1} s^{-1}, k_2 of 12 s^{-1}, and k_3 of 7 s^{-1} (derived by simulating the data in Figure 4 that were obtained with high concentrations of enzyme and oxygen), to simulate traces for each O_2 concentration and taurine-αKG-Fe^{II}TauD concentration (approximated on the basis of the Fe^{II} concentration). The simulated traces were then fit to two exponentials, and the derived rate constants were plotted as in the lower panel of Figure 6. The plot (shown in Figure S1 of the Supporting Information) nicely reproduced the major features of the data; i.e., k_2 was unaffected by the O_2 concentration, except when it approached the enzyme concentration, and k_1 was linear with the O_2 concentration with a nonzero intercept. Somewhat better fits to the intercept and slope of the apparent rate constants of Fe^{IV}-oxo formation were obtained by reducing k_3 to 2.5 s^{-1} (Figure S2 of the Supporting Information). Our ability to accurately mimic the data shown in the lower panel of Figure 6 by using Scheme 3 provides support for this kinetic scheme.

Stopped-flow spectroscopic analyses of wild-type TauD were extended to assess the reaction of the enzyme with alternative substrates. Significantly, the absorbance change believed to be associated with the Fe^{IV}-oxo intermediate was not observed when using either MOPS or PSA (Figure 7). A reasonable interpretation of these results is that the reaction exhibits a small k_1 with these slow substrates, so that significant levels of the intermediate never develop.

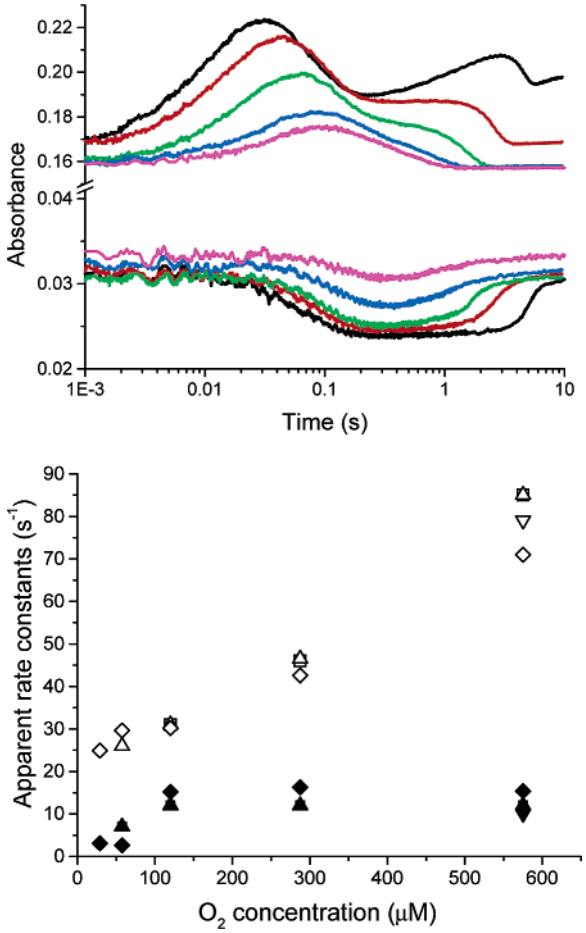

FIGURE 6: Oxygen concentration dependence of the rates of formation and decay of the Fe^{IV}-oxo species. (Upper panel) Absorbance changes at 320 nm (upper traces) and 520 nm (lower traces) observed upon mixing 100 μM wild-type TauD subunit, 100 μM Fe^{II}, 10 mM αKG, and 10 mM taurine in 25 mM Tris buffer at pH 8.0, with an equal volume of buffer equilibrated with 1.15 mM (black), 0.575 mM (red), 0.242 mM (green), 0.115 mM (navy blue), or 0.058 mM (magenta) oxygen (1 cm path length using the Hi-Tech instrument). (Lower panel) Apparent rate constants of Fe^{IV}-oxo formation and decay as a function of the oxygen concentration after mixing. The observed rate constants of Fe^{IV}-oxo formation (◇, △, □ and ▽) and decay (◆, ▲, ■ and ▼) were obtained using 50 μM TauD (◆ and ◇), 55 μM TauD (▲ and △), 125 μM TauD (■ and □), and 250 μM TauD (▼ and ▽).

Stopped-Flow Analysis of TauD Variants. Anaerobic samples of selected TauD variants were incubated with Fe^{II}, αKG, and taurine at pH 8.0, mixed with buffer containing 0.242 or 1.15 mM oxygen, and monitored at 320 nm by stopped-flow UV−visible spectroscopy at 4 °C (a selection of traces are shown in Figure 8). We presume that the intermediates observed in the mutant proteins are the same as that seen in the wild-type enzyme. The apparent first-order rate constants k_1 and k_2 for Fe^{IV}-oxo formation and decay in these variants (derived from multiple experiments) are provided in Table 3 at both oxygen concentrations. In addition, we compare the apparent second-order rate constants of these samples, calculated as the slopes of plots of k_1 versus O_2 concentrations for the two points. In the case of the wild-type enzyme, we found that the apparent second-order rate constant underestimates the true second-order rate constant by ~37%; similar underestimation is also likely to apply to the variants. The results indicate that the apparent

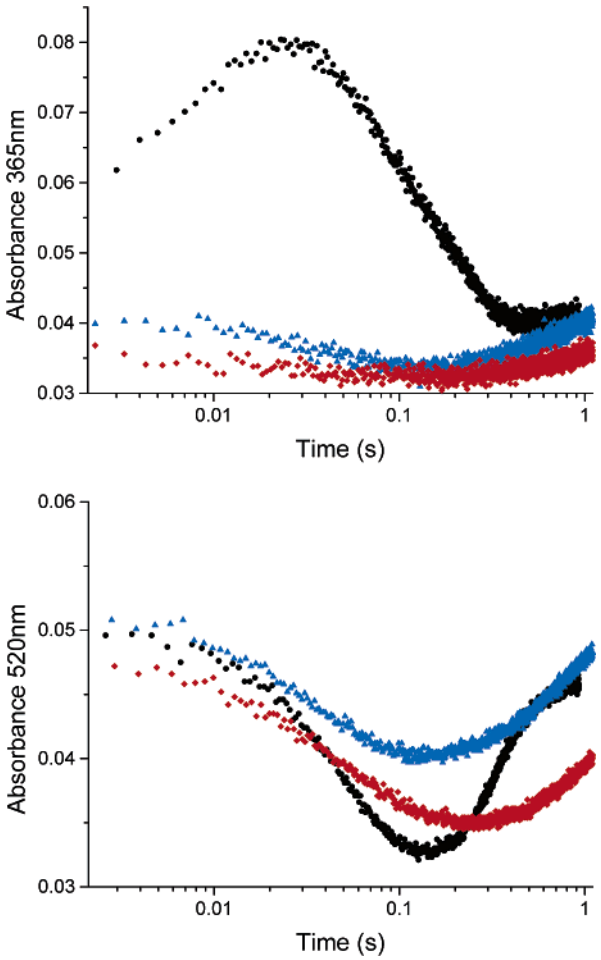

FIGURE 7: Stopped-flow UV−visible kinetic data for the reaction of αKG-Fe^{II}TauD plus alternative sulfonates with oxygen. Spectra were obtained after mixing 1.1 mM TauD subunit, 1.0 mM Fe^{II}, 10 mM αKG, and 10 mM sulfonate in 25 mM Tris buffer at pH 8.0, with buffer containing 1.15 mM oxygen at 4 °C (0.4 cm path length using the Olis instrument). The absorbance changes are presented from 5 to 800 ms at (upper panel) 365 nm and (lower panel) 520 nm for experiments utilizing taurine (black), MOPS (blue), and PSA (red).

second-order k_1 can vary from 6.4×10^4 to 1.87×10^5 M^{-1} s^{-1}, corresponding to a variation of the true second-order rate constant from 8.7×10^4 to 2.56×10^5 M^{-1} s^{-1}. The S158A protein exhibited the longest-lived intermediate of those tested and generated the highest concentration of the presumed Fe^{IV}-oxo species, especially at the lower oxygen concentration, primarily because of its small k_2 (with the large k_1 also contributing). In contrast, in buffer containing 0.575 mM oxygen, the largest k_2 was associated with the W98I sample, resulting in the shortest-lived intermediate observed. The Y73I protein exhibited the largest k_1 value of all samples investigated. The kinetics of the N97A and Y256F variants closely resembled that of the wild-type protein, but significantly less of the intermediate was observed. Finally, none of the intermediate could be observed in the N95D or N95A variants.

DISCUSSION

Steady-State Kinetics of Wild-Type and Variant Forms of TauD Using Alternative Sulfonates. The present work supports predictions based on crystallographic data (Figure 1) that His 70 and Arg 270 are critical to recognition of the taurine sulfonate group. The taurine-αKG-Fe^{II}TauD structure (*26*, *27*) reveals that His 70 lies 2.32 Å from the closest sulfonate oxygen atom, while the two guanidino nitrogens of Arg 270 are 2.73 and 3.16 Å from a second sulfonate oxygen (with the third sulfonate oxygen interacting with the backbone N−H of Val 102 at a distance of 2.68 Å). Loss of

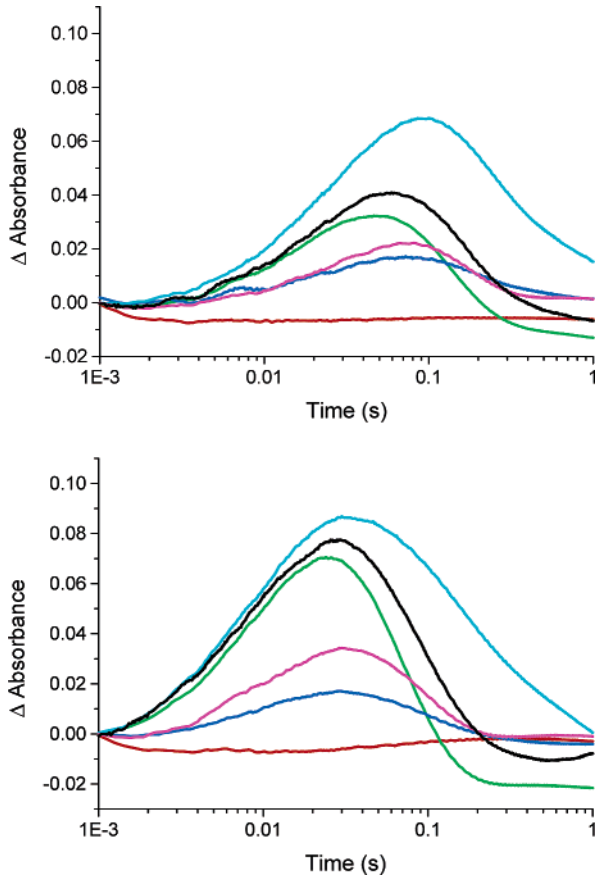

FIGURE 8: Overlay of the stopped-flow UV−visible kinetic traces of wild-type TauD and selected variants. The traces obtained with the Hi-Tech instrument illustrate the differences observed at 320 nm during the reaction of TauD and its variants (250 μM enzyme, 250 μM Fe^{II}, 10 mM αKG, and 10 mM taurine in 25 mM Tris at pH 8.0), mixed with an equal volume of buffer containing 0.242 mM (top) or 1.15 mM (bottom) oxygen. The traces correspond to the wild-type enzyme (black) and the N95D (red), N97A (dark blue), W98I (green), S158A (blue), and Y256F (magenta) variants.

Table 3: Apparent Rate Constants Associated with Fe^{IV}-oxo Formation and Decay in Wild-Type TauD and Selected Variants[a]

	0.121 mM O_2		0.575 mM O_2		
TauD species	k_1 (s^{-1})	k_2 (s^{-1})	k_1 (s^{-1})	k_2 (s^{-1})	k_1[b] (10^5 M^{-1} s^{-1})
wild type	31 ± 4	12 ± 4	85 ± 6	12 ± 3	1.19 ± 0.23
Y73I	53 ± 5	20 ± 7	138 ± 7	16 ± 4	1.87 ± 0.26
Y73S	36 ± 3	9 ± 1	77 ± 4	15 ± 6	0.90 ± 0.15
N95A/N95D[c]					
N97A	28 ± 3	6 ± 1	78 ± 8	10 ± 3	1.10 ± 0.24
W98I	38 ± 3	9 ± 3	67 ± 4	19 ± 2	0.64 ± 0.15
S158A	28 ± 2	3 ± 2	101 ± 2	5 ± 1	1.61 ± 0.09
Y256F	21 ± 3	10 ± 2	68 ± 6	11 ± 3	1.03 ± 0.20

[a] Rates as determined by KinetAsyst3 and the Marquardt algorithm of Program A. [b] The apparent second-order rate constants are derived from the slopes of plots of k_1 versus the oxygen concentration. Simulations have shown that this value underestimates the true second-order rate constant by about 37% for the wild-type enzyme. [c] No intermediate detected.

key interactions in the R270K and H70A variants results in inactive enzymes (Table 1). On the basis of their ability to form both the αKG-Fe^{II}TauD chromophore (at 530 nm) and a transient tyrosyl radical (detected at 408 nm), these proteins still fold properly, bind αKG, and activate oxygen. In contrast, these proteins fail to undergo a taurine-dependent UV−visible spectroscopic change because of their inability to bind the substrate.

Although Tyr 73 and Ser 158 originally were proposed to directly interact with the amine group of taurine (*26*), a higher resolution structure (*27*) reveals that these residues are too distant (3.94 and 4.04 Å) to form hydrogen bonds with the amine nitrogen. The closest residue to the taurine amine is Asn 95 (3.45 Å to its amide oxygen), while His 99 (a metal ligand), Asn 97, and Asp 94 are 4.24, 4.58, and 4.84 Å away from taurine, respectively. Substitution of Asn 95 with Ala or Asp leads to the greatest increase (∼25-fold at pH 8.0) in K_m (Table 1), although 4- and 11-fold increases were observed for the Y73I and Y73S variants. Of the mutant proteins examined, the N95A and N95D enzymes demonstrated the greatest decreases in k_{cat}, again highlighting the importance of Asn 95 in properly positioning the substrate for catalysis.

Additional insights into TauD reactivity were derived from steady-state kinetic analyses with alternative substrates. The K_m values for taurine, MOPS, and PSA reported here at pH 6.9 are 1.4-, 2-, and 2.9-fold greater than those initially reported (*22*), and additional small variations were noted upon changing to pH 8.0. Furthermore, the k_{cat} values determined here for utilization of taurine, MOPS, and PSA at pH 6.9 are 4.7-fold greater, equivalent, and 2-fold greater, respectively, than those originally reported (*22*). These greater values likely reflect a better quality enzyme obtained here and the use of single-time-point assays in the prior work that did not account for time-dependent enzyme inactivation. In contrast to the published statement that maximal activity was observed at pH 6.9 for this enzyme (*22*), we find larger k_{cat} and k_{cat}/K_m values for each of the three substrates at pH 8.0 compared to pH 6.9. Substitution of Ala for Ser 158 or Asn 97 is likely to increase the size and hydrophobicity of the taurine-binding site. As expected, both mutant enzymes displayed relative decreases in K_m using the more hydrophobic substrate PSA compared to taurine. At the same time, the S158A variant exhibited a large increase in the taurine K_m, especially at the lower pH value, suggesting that Ser 158 assists in binding the protonated amine in this substrate. No comparable amine is present in PSA, and MOPS contains only a tertiary amine.

Transient Kinetics of Wild-Type TauD. Wild-type enzyme kinetics data were simulated according to the three-step mechanism of Scheme 3. Best fits were obtained with apparent rate constants (158 000 M^{-1} s^{-1} and 12 and 7 s^{-1} at pH 8.0 and 4 °C) that are closely similar to those (145 000 M^{-1} s^{-1} and 13.7 and 2.5 s^{-1} at pH 7.6 and 5 °C) previously reported by Price et al. (*36*) using the same general approach. These parallel results provide assurance that we are studying the same process as the other investigators. None of the rate constants exhibited a detectable solvent isotope effect, suggesting that no protons from the solvent are involved in any of the observed steps. The lack of solvent deuterium isotope effect on the rate constant associated with Fe^{IV}-oxo formation means that protonation of the preceding oxygen-bound complex is not the rate-determining step, in contrast to the case of cytochrome P450 (*25*).

The generally reported mechanism of this family of enzymes, shown in Scheme 2, implies that formation of the Fe^{IV}-oxo species **F** proceeds from **C** to **D** and **E**. Perhaps surprisingly, this complex process appears to occur in a single phase (Figures 4, 5, and 8). One explanation is that upon forming **D** (or a reversible precursor of **D**) subsequent reactions leading to **F** are very fast. Although unlikely, another possibility is that species such as **D** or **E** might not have easily identifiable spectral features.

The studies described here represent the first effort to characterize the oxygen dependence of Fe^{IV}-oxo formation in any Fe^{II}/αKG-dependent oxygenase. Our results were compatible with the three-step Scheme 3, where k_1 (1.58×10^5 M^{-1} s^{-1}) is the second-order rate constant for the reaction of oxygen with taurine-αKG-Fe^{II}TauD. By way of comparison, a second-order rate constant of 1.43×10^5 M^{-1} s^{-1} was determined for formation of an unidentified intermediate in the mechanistically related enzyme 4-hydroxyphenylpyruvate dioxygenase (*48*).

The reactions with the alternative sulfonates MOPS and PSA were catalyzed by αKG-Fe^{II}TauD at rates that were 28 and 14% of that with taurine (at pH 8.0); however, turnover of these substrates did not result in accumulation of detectable amounts of the intermediate (Figure 7). The products formed from these substrates are sulfite and the corresponding aldehyde, analogous to the reaction with taurine. Therefore, we presume that an Fe^{IV}-oxo species occurs during catalysis, as in Scheme 2. With MOPS and PSA, the lack of observable intermediate must be due to a small ratio of the apparent first-order rate constants k_1/k_2 (Scheme 3). We estimate that the turnover numbers for PSA and MOPS at 4 °C are 0.6 and 0.3 s^{-1}. If k_2 remains at ∼12 s^{-1} (as for taurine), k_1 could be as low as 1 s^{-1}, which would account for no observable Fe^{IV}-oxo species. As in the case of taurine, the rate-determining step for turnover of these alternative substrates must occur after the decay of the intermediate.

Transient Kinetics of Variant TauD Proteins. The kinetics of the oxygen reaction with taurine-αKG-Fe^{II}TauD were affected by substitution of residues near the active site. The W98I variant is rather remarkable in exhibiting a higher k_{cat} and has a greater resistance to inactivation (smaller k_{inact}) than that of the wild-type enzyme (Table 1). As depicted in Figure 8, the rate of formation of the Fe^{IV}-oxo species in this protein was similar to that of the wild-type enzyme, but the decay of the intermediate was significantly faster (note the large k_2 in Table 3 at high oxygen concentrations) implying a faster substrate hydroxylation step. We speculate that the rapid oxygen insertion into the substrate (k_2 in Table 3) at least partially accounts for the enhanced resistance to inactivation of the protein by competing more effectively with the autoinactivation reaction, a process that involves abstraction of a hydrogen atom from a nearby tyrosine (*46*, *47*) when no substrate is present. Restated, we suggest that the W98I enzyme rapidly carries out substrate hydroxylation resulting in less protein self-oxidation. The S158A variant exhibits only small changes in its steady-state kinetics, but as revealed by the stopped-flow studies, its k_2 is much smaller than that for the wild-type enzyme. These observations imply a slower substrate hydroxylation step and suggest that one function of Ser 158 is to help orient the taurine appropriately

for catalysis. Because of the longer lifetime and larger proportion of the intermediate observed in this protein, the S158A variant may be particularly useful for future characterization of the Fe^{IV}-oxo properties. The Y73I variant is notable for its large k_1 and k_2. We speculate that removal of the aromatic group, while retaining a hydrophobic environment, enhances oxygen access to the active site, thus placing Tyr 73 along the route of oxygen transfer. The lower k_1 observed in the Y73S variant is consistent with this notion, because decreased hydrophobicity along the oxygen transfer route would hinder the rate of oxygen binding. This substitution also results in an 11-fold increase in the K_m of taurine. The N95D and N95A variants exhibit significant decreases in k_{cat}, large increases in the K_m of taurine, and minimal changes to the spectrum of the αKG-bound proteins upon binding taurine (Figure 2). No evidence for an Fe^{IV}-oxo intermediate was observed in the stopped-flow traces, but this species is likely to be used during catalysis. We speculate that the substitution of this Asn by Asp or Ala may impede conversion of the six-coordinate intermediate **B** to the five-coordinate intermediate **C** (Scheme 2), thus resulting in a greatly reduced rate of Fe^{IV}-oxo formation. The steady-state and transient kinetic properties of the N97A and Y256F variants are much like those of the wild-type enzyme, yet the intensity of the presumed Fe^{IV}-oxo species is smaller. We have no clear understanding of why the absorbance intensity of this intermediate would be less but suggest that it may involve subtle conformational changes of the metallocenter. Overall, these stopped-flow studies of TauD variants have begun to identify how the protein environment can influence the kinetics associated with the Fe^{IV}-oxo intermediate, and they set the stage for further investigations to define the mechanism of catalysis.

ACKNOWLEDGMENT

We thank Shelagh Ferguson-Miller for use of her stopped-flow instrument, Tina Müller for help with collecting some of the stopped-flow data, Tim Egbert for assistance with some enzyme purifications and assays, Scott Mulrooney for helpful discussions, and the reviewers for their very helpful comments about the kinetics and experimental suggestions.

SUPPORTING INFORMATION AVAILABLE

Two figures of apparent rate constants derived from simulations of the kinetics for varied oxygen and taurine-αKG-Fe^{II}TauD concentrations. This material is available free of charge via the Internet at http://pubs.acs.org.

REFERENCES

1. Hausinger, R. P. (2004) Fe^{II}/α-ketoglutarate-dependent hydroxylases and related enzymes, *Crit. Rev. Biochem. Mol. Biol. 39*, 21−68.
2. Prescott, A. G., and Lloyd, M. D. (2000) The iron(II) and 2-oxoacid-dependent dioxygenases and their role in metabolism, *Nat. Prod. Rep. 17*, 367−383.
3. Trewick, S. C., Henshaw, T. F., Hausinger, R. P., Lindahl, T., and Sedgwick, B. (2002) Oxidative demethylation by *Escherichia coli* AlkB directly reverts DNA base damage, *Nature 419*, 174−178.
4. Aas, P. A., Otterlei, M., Falnes, P. O., Vagbe, C. B., Skorpen, F., Akbari, M., Sundheim, O., Bjoras, M., Slupphaug, G., Seeberg, E., and Krokan, H. E. (2003) Human and bacterial oxidative demethylases repair alkylation damage in both RNA and DNA, *Nature 421*, 859−863.
5. Kivirikko, K. I., and Pihlajaniemi, T. (1998) Collagen hydroxylases and the protein disulfide isomerase subunit of prolyl 4-hydroxylase, *Adv. Enzymol. Relat. Areas Mol. Biol. 72*, 325−398.
6. Ivan, M., Kondo, K., Yang, H., Kim, W., Valiando, J., Ohh, M., Salic, A., Asara, J. M., Lane, W. S., and Kaelin, W. G., Jr. (2001) HIFα targeted for VHL-mediated destruction by proline hydroxylation: Implications for O_2 sensing, *Science 292*, 464−467.
7. Jaakkola, P., Mole, D. R., Tian, Y.-M., Wilson, M. I., Gielbert, J., Gaskell, S. J., von Kriegsheim, A., Hebestreit, H. F., Mukherji, M., Schofield, C. J., Maxwell, P. H., Pugh, C. W., and Ratcliffe, P. J. (2001) Targeting of HIF-α to the von Hippel−Lindau ubiquitylation complex by O_2-regulated prolyl hydroxylation, *Science 292*, 468−472.
8. Dann, C. E., III, Bruick, R. K., and Deisenhofer, J. (2002) Structure of a factor-inhibiting hypoxia-inducible factor 1: An essential asparaginyl hydroxylase involved in the hypoxic response pathway, *Proc. Natl. Acad. Sci. U.S.A. 99*, 15351−15356.
9. Zhang, Z., Ren, J., Stammers, D. K., Baldwin, J. E., Harlos, K., and Schofield, C. J. (2000) Structural origins of the selectivity of the trifunctional oxygenase clavaminic acid synthase, *Nat. Struct. Biol. 7*, 127−133.
10. Clifton, I. J., Hsueh, L.-C., Baldwin, J. E., Harlos, K., and Schofield, C. J. (2001) Structure of proline 3-hydroxylase. Evolution of the family of 2-oxoglutarate dependent dioxygenases, *Eur. J. Biochem. 268*, 6625−6636.
11. Lukacin, R., Groning, I., Pieper, U., and Matern, U. (2000) Site-directed mutagenesis of the active site serine290 in flavanone 3β-hydroxylase from *Petunia hybrida*, *Eur. J. Biochem. 267*, 853−860.
12. Hedden, P., and Phillips, A. L. (2000) Gibberellin metabolism: New insights revealed by the genes, *Trend Plant Sci. 5*, 523−528.
13. De Carolis, E., Chan, F., Balsevich, J., and De Luca, V. (1990) Isolation and characterization of a 2-oxoglutarate dependent dioxygenase involved in the second-to-last step in vindoline biosynthesis, *Plant Physiol. 94*, 1323−1329.
14. Hashimoto, T., and Yamada, Y. (1987) Purification and characterization of hyoscyamine 6β-hydroxylase from root cultures of *Hyoscyamus niger* L. Hydroxylase and epoxidase activities of enzyme preparations, *Eur. J. Biochem. 164*, 277−285.
15. Jansen, G. A., Mihalik, S. J., Watkins, P. A., Jakobs, C., Moser, H. W., and Wanders, R. J. A. (1998) Characterization of phytanoyl-coenzyme A hydroxylase in human liver and activity measurements in patients with peroxisomal disorders, *Clin. Chim. Acta 271*, 203−211.
16. Fukumori, F., and Hausinger, R. P. (1993) Purification and characterization of 2,4-dichlorophenoxyacetate/α-ketoglutarate dioxygenase, *J. Biol. Chem. 268*, 24311−24317.
17. Valegård, K., Terwisscha van Scheltinga, A. C., Lloyd, M. D., Hara, T., Ramaswamy, S., Perrakis, A., Thompson, A., Lee, W.-J., Baldwin, J. E., Schofield, C. J., Hajdu, J., and Andersson, I. (1998) Structure of a cephalosporin synthase, *Nature 394*, 805−809.
18. Wilmouth, R. C., Turnbull, J. J., Welford, R. W. D., Clifton, I. J., Prescott, A. G., and Schofield, C. J. (2002) Structure and mechanism of anthocyanidin synthase from *Arabidopsis thaliana*, *Structure 10*, 93−103.
19. Roach, P. L., Clifton, I. J., Hensgens, C. M. H., Shibata, N., Schofield, C. J., Hajdu, J., and Baldwin, J. E. (1997) Structure of isopenicillin *N* synthase complexed with substrate and the mechanism of penicillin formation, *Nature 387*, 827−830.
20. Zhou, J., Rocklin, A. M., Lipscomb, J. D., Que, L., Jr., and Solomon, E. I. (2002) Spectroscopic studies of 1-aminocyclopropane-1-carboxylic acid oxidase: Molecular mechanism and CO_2 activation in the biosynthesis of ethylene, *J. Am. Chem. Soc. 124*, 4602−4609.
21. Clifton, I. J., Doan, L. X., Sleeman, M. C., Topf, M., Suzuki, H., Wilmouth, R. C., and Schofield, C. J. (2003) Crystal structure of carbapenem synthase (CarC), *J. Biol. Chem. 278*, 20843−20850.
22. Eichhorn, E., van der Ploeg, J. R., Kertesz, M. A., and Leisinger, T. (1997) Characterization of α-ketoglutarate-dependent taurine dioxygenase from *Escherichia coli*, *J. Biol. Chem. 272*, 23031−23036.
23. Solomon, E. I., Brunold, T. C., Davis, M. I., Kemsley, J. N., Lee, S.-K., Lehnert, N., Neese, F., Skulan, A. J., Yang, Y.-S., and Zhou, J. (2000) Geometric and electronic structure/function correlations in non-heme iron enzymes, *Chem. Rev. 100*, 235−349.
24. Hanauske-Abel, H. M., and Günzler, V. (1982) A stereochemical concept for the catalytic mechanism of prolylhydroxylase. Ap-

plicability to classification and design of inhibitors, *J. Theor. Biol. 94*, 421−455.
25. Sono, M., Roach, M. P., Coulter, E. D., and Dawson, J. H. (1996) Heme-containing oxygenases, *Chem. Rev. 96*, 2841−2887.
26. Elkins, J. M., Ryle, M. J., Clifton, I. J., Dunning Hotopp, J. C., Lloyd, J. S., Burzlaff, N. I., Baldwin, J. E., Hausinger, R. P., and Roach, P. L. (2002) X-ray crystal structure of *Escherichia coli* taurine/α-ketoglutarate dioxygenase complexed to ferrous iron and substrates, *Biochemistry 41*, 5185−5192.
27. O'Brien, J. R., Schuller, D. J., Yang, V. S., Dillard, B. D., and Lanzilotta, W. N. (2003) Substrate-induced conformational changes in *Escherichia coli* taurine/α-ketoglutarate dioxygenase and insight into the oligomeric structure, *Biochemistry 42*, 5547−5554.
28. Lee, H. J., Lloyde, M. D., Clifton, I. J., Baldwin, J. E., and Schofield, C. J. (2001) Kinetic and crystallographic studies on deacetoxycephalosporin C synthase (DAOCS), *J. Mol. Biol. 308*, 937−948.
29. Zhang, Z., Ren, J.-s., Harlos, K., McKinnon, C. H., Clifton, I. J., and Schofield, C. J. (2002) Crystal structure of a clavaminate synthase-Fe^{II}-2-oxoglutarate-substrate-NO complex: Evidence for metal centred rearrangements, *FEBS Lett. 517*, 7−12.
30. Elkins, J. M., Hewitson, K. S., McNeill, L. A., Seibel, J. F., Schlemminger, I., Pugh, C. W., Ratcliffe, P. J., and Schofield, C. J. (2003) Structure of factor-inhibiting hypoxia-inducible factor (HIF) reveals mechanism of oxidative modification of HIF-1α, *J. Biol. Chem. 278*, 1802−1806.
31. Müller, I., Kahnert, A., Pape, T., Sheldrick, G. M., Meyer-Klaucke, W., Dierks, T., Kertesz, M., and Usòn, I. (2004) Crystal structure of the alkylsulfatase AtsK: Insights into the catalytic mechanism of the Fe^{II} α-ketoglutarate-dependent dioxygenase superfamily, *Biochemistry 43*, 3075−3088.
32. Ryle, M. J., Padmakumar, R., and Hausinger, R. P. (1999) Stopped-flow kinetic analysis of *Escherichia coli* taurine/α-ketoglutarate dioxygenase: Interactions with α-ketoglutarate, taurine, and oxygen, *Biochemistry 38*, 15278−15286.
33. Pavel, E. G., Zhou, J., Busby, R. W., Gunsior, M., Townsend, C. A., and Solomon, E. I. (1998) Circular dichroism and magnetic circular dichroism spectroscopic studies of the non-heme ferrous active site in clavaminate synthase and its interaction with α-ketoglutarate cosubstrate, *J. Am. Chem. Soc. 120*, 743−753.
34. Zhou, J., Kelly, W. L., Bachmann, B. O., Gunsior, M., Townsend, C. A., and Solomon, E. I. (2001) Spectroscopic studies of substrate interactions with clavaminate synthase 2, a multifunctional α-KG-dependent non-heme iron enzyme: Correlation with mechanisms and reactivities, *J. Am. Chem. Soc. 123*, 7388−7398.
35. Ho, R. Y. N., Mehn, M. P., Hegg, E. L., Liu, A., Ryle, M. A., Hausinger, R. P., and Que, L., Jr. (2001) Resonance Raman studies of the $iron^{II}$-α-keto acid chromophore in model and enzyme complexes, *J. Am. Chem. Soc. 123*, 5022−5029.
36. Price, J. C., Barr, E. W., Tirupati, B., Bollinger, J. M., Jr., and Krebs, C. (2003) The first direct characterization of a high-valent iron intermediate in the reaction of an α-ketoglutarate-dependent dioxygenase: A high-spin Fe^{IV} complex in taurine/α-ketoglutarate dioxygenase (TauD) from *Escherichia coli*, *Biochemistry 42*, 7497−7508.
37. Price, J. C., Barr, E. W., Glass, T. E., Krebs, C., and Bollinger, J. M., Jr. (2003) Evidence for hydrogen abstraction from C1 of taurine by the high-spin Fe^{IV} intermediate detected during oxygen activation by taurine:α-ketoglutarate dioxygenase (TauD), *J. Am. Chem. Soc. 125*, 13008−13009.
38. Proshlyakov, D. A., Henshaw, T. F., Monterosso, G. R., Ryle, M. J., and Hausinger, R. P. (2004) Direct detection of oxygen intermediates in the non-heme Fe enzyme taurine/α-ketoglutarate dioxygenase, *J. Am. Chem. Soc. 126*, 1022−1023.
39. Riggs-Gelasco, P. J., Price, J. C., Guyer, R. B., Brehm, J. H., Barr, E. W., Bollinger, J. M., Jr., and Krebs, C. (2004) EXAFS spectroscopic evidence for an Fe═O unit in the Fe^{IV} intermediate observed during oxygen activation by taurine:α-ketoglutarate dioxygenase, *J. Am. Chem. Soc. 126*, 8108−8109.
40. Borowski, T., Bassan, A., and Siegbahn, P. E. M. (2004) Mechanism of dioxygen activation in 2-oxoglutarate-dependent enzymes: A hybrid DFT study, *Chem. Eur. J. 10*, 1031−1041.
41. Rohde, J.-U., In, J.-H., Lim, M. H., Brennessel, W. W., Bukowski, M. R., Stubna, A., Münck, E., and Que, L., Jr. (2003) Crystallographic and spectroscopic characterization of a nonheme Fe^{IV}═O complex, *Science 299*, 1037−1039.
42. Lim, M. H., Rohde, J.-U., Stubna, A., Bukowski, M. R., Costas, M., Ho, R. Y. N., Münck, E., Nam, W., and Que, L., Jr. (2003) An Fe^{IV}═O complex of a tetradentate tripodal nonheme ligand, *Proc. Natl. Acad. Sci. U.S.A. 100*, 3665−3670.
43. Decker, A., Rohde, J.-U., Que, L., Jr., and Solomon, E. I. (2004) Spectroscopic and quantum chemical characterization of the electronic structure and bonding in a non-heme Fe^{IV}═O complex, *J. Am. Chem. Soc. 126*, 5378−5379.
44. Liu, A., Ho, R. Y. N., Que, L., Jr., Ryle, M. J., Phinney, B. S., and Hausinger, R. P. (2001) Alternative reactivity of an α-keto-glutarate-dependent iron(II) oxygenase: Enzyme self-hydroxylation, *J. Am. Chem. Soc. 123*, 5126−5127.
45. Henshaw, T. F., Feig, M., and Hausinger, R. P. (2004) Aberrant activity of the DNA repair enzyme AlkB, *J. Inorg. Biochem. 98*, 856−861.
46. Ryle, M. J., Liu, A., Muthukumaran, R. B., Ho, R. Y. N., Koehntop, K. D., McCracken, J., Que, L., Jr., and Hausinger, R. P. (2003) O_2- and α-ketoglutarate-dependent tyrosyl radical formation in TauD, an α-keto acid-dependent non-heme iron dioxygenase, *Biochemistry 42*, 1854−1862.
47. Ryle, M. J., Koehntop, K. D., Liu, A., Que, L., Jr., and Hausinger, R. P. (2003) Interconversion of two oxidized forms of TauD, a non-heme iron hydroxylase: Evidence for bicarbonate binding, *Proc. Natl. Acad. Sci. U.S.A. 100*, 3790−3795.
48. Johnson-Winters, K., Purpero, V. M., Kavana, M., Nelson, T., and Moran, G. R. (2003) (4-Hydroxyphenyl)pyruvate dioxygenase from *Streptomyces avermitilis*: The basis for ordered substrate addition, *Biochemistry 42*, 2072−2080.
49. Brownlee, J. M., Johnson-Winters, K., Harrison, D. H. T., and Moran, G. R. (2004) Structure of the ferrous form of (4-hydroxyphenyl)pyruvate dioxygenase from *Streptomyces avermitilis* in complex with the therapeutic herbicide, NTBC, *Biochemistry 43*, 6370−6377.
50. Borowski, T., Bassan, A., and Siegbahn, P. E. M. (2004) 4-Hydroxyphenylpyruvate dioxygenase: A hybrid density functional study of the catalytic reaction mechanism, *Biochemistry 43*, 12331−12342.
51. Moran, G. R. (2005) 4-Hydroxyphenylpyruvate dioxygenase, *Arch. Biochem. Biophys. 433*, 117−128.
52. Saari, R. E., and Hausinger, R. P. (1998) Ascorbic acid-dependent turnover and reactivation of 2,4-dichlorophenoxyacetic acid/α-ketoglutarate dioxygenase using thiophenoxyacetic acid, *Biochemistry 37*, 3035−3042.
53. Patil, P. V., and Ballou, D. P. (2000) The use of protocatechuate dioxygenase for maintaining anaerobic conditions in biochemical experiments, *Anal. Biochem. 286*, 187−192.
54. Matheson, I. B. C., and De Sa, R. J. (1990) Robust multivariate analysis applied to separation of components in absorption spectra, *Comput. Chem. 14*, 157−164.
55. Schowen, K. B., and Schowen, R. L. (1982) Solvent isotope effects of enzyme systems, *Methods Enzymol. 87*, 551−606.
56. Bevington, P. R. (1969) in *Data Reduction and Error Analysis for the Physical Sciences*, pp 235−242, McGraw−Hill, Inc., New York.

BI048746N